PAPER

Inferring divertor plasma properties from hydrogen Balmer and Paschen series spectroscopy in JET-ILW

To cite this article: B.A. Lomanowski *et al* 2015 *Nucl. Fusion* **55** 123028

IOP Publishing | International Atomic Energy Agency Nuclear Fusion

Nucl. Fusion **55** (2015) 123028 (14pp) doi:10.1088/0029-5515/55/12/123028

Inferring divertor plasma properties from hydrogen Balmer and Paschen series spectroscopy in JET-ILW

B.A. Lomanowski[1], A.G. Meigs[2], R.M. Sharples[1], M. Stamp[2], C. Guillemaut[3] and JET Contributors[a]

EUROfusion Consortium, JET, Culham Science Centre, Abingdon OX14 3DB, UK
[1] Centre for Advanced Instrumentation, Department of Physics, Durham University, Durham DH1 3LE, UK
[2] EURATOM/CCFE Fusion Association, Culham Science Centre, Abingdon OX14 3DB, UK
[3] Instituto de Plasmas e Fusão Nuclear, Instituto Superior Técnico, Universidade Lisboa, 1049-001 Lisboa, Portugal

E-mail: b.a.lomanowski@durham.ac.uk

Received 1 May 2015, revised 18 September 2015
Accepted for publication 21 October 2015
Published 19 November 2015

Abstract

A parametrised spectral line profile model is formulated to investigate the diagnostic scope for recovering plasma parameters from hydrogenic Balmer and Paschen series spectroscopy in the context of JET-ILW divertor plasmas. The separate treatment of Zeeman and Stark contributions in the line model is tested against the PPP-B code which accounts for their combined influence on the spectral line shape. The proposed simplified model does not fully reproduce the Stark–Zeeman features for the α and β transitions, but good agreement is observed in the line width and wing profiles, especially for $n > 5$. The line model has been applied to infer radial density profiles in the JET-ILW divertor with generally good agreement between the D $5 \rightarrow 2$, $5 \rightarrow 3$, $6 \rightarrow 2$, $7 \rightarrow 2$ and $9 \rightarrow 2$ lines for high recycling and detached conditions. In an L-mode detached plasma pulse the Langmuir probe measurements typically underestimated the density by a factor 2–3 and overestimated the electron temperature by a factor of 5–10 compared to spectroscopically derived values. The line model is further used to generate synthetic high-resolution spectra for low-n transitions to assess the potential for parameter recovery using a multi-parametric fitting technique. In cases with 4 parameter fits with a single Maxwellian neutral temperature component the D $4 \rightarrow 3$ line yields the best results with parameter estimates within 10% of the input values. For cases with 9 parameter fits inclusive of a multi-component neutral velocity distribution function the quality of the fits is degraded. Simultaneous fitting of the D $3 \rightarrow 2$ and $4 \rightarrow 3$ profiles improves the fit quality significantly, highlighting the importance of complementary spectroscopic measurements for divertor plasma emission studies.

Keywords: plasma spectroscopy, tokamak divertor diagnostics, spectral line profiles

(Some figures may appear in colour only in the online journal)

1. Introduction

The interpretation of hydrogen isotope line emission spectra in tokamak divertors is of great interest in advancing the understanding of plasma exhaust and divertor physics. This is especially relevant for detachment experiments in preparation for the ITER baseline scenario [1] for which operation at high density and partial detachment is mandatory for reducing heat loads on plasma facing components. Reliable measurements of plasma parameters such as density and electron temperature at and away from the divertor targets are necessary for

[a] See the appendix of Romanelli *et al* 2014 *Proc. of the 25th IAEA Fusion Energy Conf. (Saint Petersburg, Russia)*

characterising the conditions under which volumetric dissipative processes act to reduce the particle and heat fluxes at the divertor targets. Application of divertor spectroscopic measurements for providing real-time spatially resolved information on the state of the detached plasma is also of interest due to increased opportunity for feedback control (e.g. [2, 3]) of the detached regime in the all metal JET ITER-like wall (JET-ILW) machine [4].

In this work we investigate the scope for plasma parameter recovery from analysis of both high-n and low-n transitions of the hydrogenic Balmer and Paschen series spectral lines. Emphasis is given on examining the diagnostic capabilities from spectral line shape interpretation using a newly formulated line profile model which captures the relevant line broadening and splitting processes. The simplifications inherent to the model make it suitable for application to batch analysis of spectroscopic data and multi-parameteric fitting techniques, while providing increased accuracy in inferring the plasma density. We first discuss the methodology and formulation of the line profile model, followed by its application to JET-ILW divertor spectroscopy data and comparison to Langmuir probe measurements, where we also provide radial profile estimates of the electron temperature. To quantify the scope for parameter recovery from complex spectral line shapes, a multi-parametric fitting analysis is then presented focusing on the low-n lines using synthetic spectra.

2. Methodology

With a suitably narrow instrumental function the spectral line profiles of the hydrogen Balmer and Paschen series lines offer a range of diagnostic possibilities for the recovery of line-of-sight (LOS) averaged plasma parameters. High resolution Ba-α ($n = 3 \rightarrow 2$) spectroscopy is typically employed for measuring the neutral velocity distribution function (VDF) in the scrape-off layer (SOL) and divertor (e.g. [5, 6]), while the broad profiles of the high-n ($n \geqslant 6$) lines dominated by Stark broadening offer a robust measure of electron density in detached or partially-detached divertor plasmas (e.g. [7–10]). In divertor plasma conditions of existing large tokamaks (e.g. JET, Asdex Upgrade) ($B < 3.0$ T, $n_e > 5 \times 10^{19}$ m^{-3} and $T_n < 10$ eV), Zeeman splitting and Doppler broadening can generally be neglected for high-n Balmer and Paschen lines. Their application as a density diagnostic relies on sufficiently high excited state population densities which become significant in high recycling conditions and when driven by three-body recombination in low temperature, high density volume recombining plasmas ($T_e < 1.5$ eV, $n_e > 10^{20}$ m^{-3}) (see e.g. [11] for overview of recombination spectra in Alcator C-Mod). A common technique (referred to herein as the standard method) for inferring plasma density from the high-n lines relies on applying a simple Voigt model for describing the line shape, for which the Gaussian component captures the instrumental broadening, and the Lorentzian component approximates the line width due to Stark broadening. Coupled to the Griem density formula, derived using the quasi-static approximation [12], this method is quite suitable for batch fitting of spectral data, but, as is shown in the next section, does not fully capture the wing profile of the Stark broadened spectral line, and neglects ion dynamics effects. For profiles of low-n lines a more general treatment of Stark, Zeeman and Doppler broadening mechanisms is required for recovery of plasma parameters.

2.1. Line profile model

The present analysis of the Balmer and Paschen series transitions is underpinned by a parametrised model of the spectral line profile in which we treat the Zeeman, Stark and Doppler effects separately and assume the convolution of the Doppler and Stark contributions to be valid in the range of JET-ILW SOL and divertor plasmas.

The basis for the magnetic effects is the ADAS603 code [13] which generates the Zeeman/Paschen-Back multiplet feature for hydrogenic species spectral lines, separated into the π and σ polarisation components, as a function of magnetic field magnitude and observation angle.

In the JET SOL, asymmetries in the LOS integrated D $3 \rightarrow 2$ Doppler broadened line profile have been observed (see [5, 14] and references therein). The local neutral VDF is influenced by multiple kinetic processes occurring due to the interaction of neutral, molecular and ion fluxes into and out of the main chamber wall. Charge exchange of relatively hot background plasma ions with cold recycled neutrals near the wall results in a broad Gaussian contribution, while reflection of fast atoms can add an asymmetric component. We employ a semi-analytic neutral VDF model [14] for describing the Doppler broadening function imposed on each Zeeman/Paschen-Back component with allowance for multiple Maxwellian and non-Maxwelian contributions. The Zeeman–Doppler profile is then convolved with a pure Stark broadened profile using a parametrisation of the Model Microfield Method (MMM) [15] wavelength detuning tabulations [16] generated for a pure hydrogen isotropic plasma. We adopted a power law of the form:

$$\Delta\lambda_{1/2}^{ij} = C_{ij}\frac{n_e^{a_{ij}}}{T_e^{b_{ij}}} \tag{1}$$

to recover the Stark full width half maximum (FWHM), $\Delta\lambda_{1/2}$ (nm), with n_e given in m^{-3} and T_e in eV, with a set of coefficients C, a, and b for each transition $i \rightarrow j$. The coefficients were determined by first interpolating the tabulated profiles for a given n_e and T_e. Due to the coarsely discretised wavelength detunings, the interpolated profile was fitted in the least-squares manner in order to more accurately estimate the Stark FWHM. We used a modified Lorentzian fitting function of the form:

$$\mathcal{L}(\gamma, \Delta\lambda) \propto \frac{1}{\Delta\lambda^{5/2} + \gamma^{5/2}}, \tag{2}$$

where $\gamma = \Delta\lambda_{1/2}/2$.

The Stark profile wing shape is attributed to the relative influence of electron and ion broadening. As one progresses up the Balmer or Paschen series to higher principal quantum

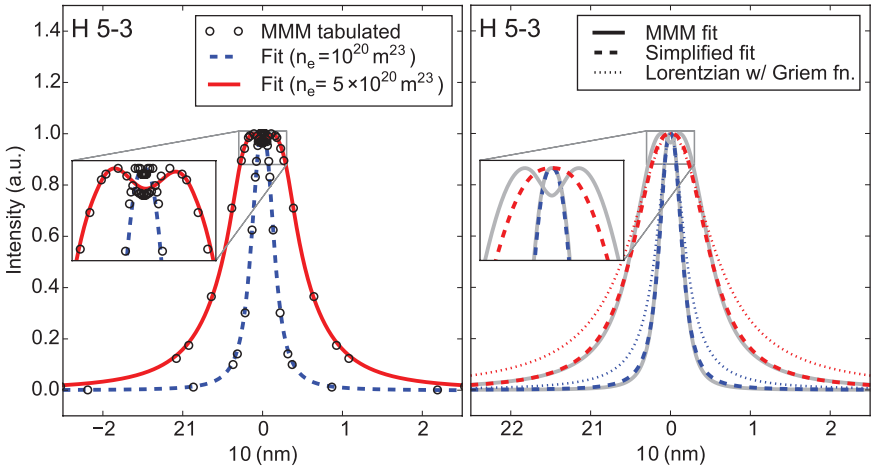

Figure 1. Left: example of three component fit to MMM tabulated H 5 → 3 line profiles. Right: comparison of the three component MMM fit to the simplified single component fit using coefficients in table 1 and equations (1) and (2). Profiles generated using the Griem density formula [12] and a Lorentzian distribution are also shown. All profiles are normalised to the peak intensity. MMM profiles are evaluated at $T_e = T_i = 1$ eV.

number n, the electron broadening contribution increases relative to the ion microfield contribution. Electron broadening in the impact approximation results in a pure Lorentzian wing decay, assuming random collisions, whereas a somewhat faster decay is typically observed due to the influence of the ion microfields (see [17] or [18] for details). For the Holtsmark microfield distribution function [19] the wing decay is $\propto \Delta\lambda^{-5/2}$. To obtain the FWHM for transitions with a shift in the central component (e.g. Ba-β ($n = 4 \rightarrow 2$), Pa-β ($n = 5 \rightarrow 3$)) the line fitting model consists of one central and two shifted modified Lorentzian components in order to resolve the central dip, as shown in figure 1 (left). This procedure was repeated across the density and temperature range of $10^{19} \leqslant n_e \leqslant 10^{21}$ m^{-3} and $1 \leqslant T_e \leqslant 10$ eV, respectively, with 200 samples. The coefficients of equation (1) were then determined based on the set of 200 FWHM values in the least-squares manner. Using this method, the parametrised FWHM error in the specified n_e and T_e range is under 10% compared with the original tabulations. Table 1 shows the recommended coefficient values for Balmer and Paschen transitions up to $n = 9$.

To simplify the Stark profile parametrisation, profiles for all transitions, including ones with a shifted central component, are recovered using the single modified Lorentzian function (equation (2)) for which $\gamma = \Delta\lambda_{1/2}/2$ is obtained with equation (1) and table 1. For the β transitions this results in a loss of resolution of the central dip, but an otherwise good fit away from the line centre, as shown in figure 1 (right). Since instrumentation and Doppler broadening will tend to blur the details of the line center it is primarily the line wings and the FWHM that encode the Stark broadening information, hence the loss in resolution of the central dip is not expected to significantly influence the recovered n_e value. Moreover, the line center features of β transitions are particularly sensitive to ion dynamic effects and, as such, are the main source of discrepancy between established Stark broadening models and experiment (e.g. [20, 21]). Figure 1 (right) also shows Stark profiles generated using the standard method (i.e. using the Griem density formula [12] coupled to a Lorentzian broadening function). The slower decay rate ($\propto \Delta\lambda^{-2}$) of the Lorentzian function results in broader profiles for divertor relevant densities, thus underestimating the inferred density values.

Table 1. Paramaterised MMM Stark profile coefficients for use with equations (1) and (2). Fit error estimates >5% shown in parentheses

H transition ($i \rightarrow j$)	C_{ij}	a_{ij}	b_{ij}
3 → 2	3.710e–18 (17.49%)	0.7665	0.064 (6.51%)
4 → 2	8.425e–18 (10.86%)	0.7803	0.050
5 → 2	1.310e–15	0.6796	0.030
6 → 2	3.954e–16 (6.24%)	0.7149	0.028
7 → 2	6.258e–16	0.7120	0.029
8 → 2	7.378e–16 (5.42%)	0.7159	0.032
9 → 2	8.947e–16 (6.88%)	0.7177	0.033
4 → 3	1.330e–16 (13.04%)	0.7449	0.045
5 → 3	6.640e–16 (7.28%)	0.7356	0.044
6 → 3	2.481e–15 (7.02%)	0.7118	0.016
7 → 3	3.270e–15	0.7137	0.029
8 → 3	4.343e–15	0.7133	0.032
9 → 3	5.588e–15 (6.81%)	0.7165	0.033

The separate calculations and subsequent convolution of the Zeeman–Doppler and Stark profiles make the model suitable for efficient application to multi-parametric nonlinear least squares minimization, but any coupling of the magnetic and electric field perturbations on the emitter is ignored. To assess the applicability of the proposed model for interpretation of diagnostic data, we employ the PPP-B code [22] as a benchmark. A reformulation of the original PPP code based on the frequency fluctuation model (FFM) [23, 24], the PPP-B code extends the calculations to magnetised plasmas by considering both the Stark and Zeeman perturbations on the evolution operator of the emitter, and has been validated with full numerical simulations of the line shape function in the radiative dipole approximation for a set of ions and electrons moving along straight trajectories (see [22] and references therein). The line profile calculation in

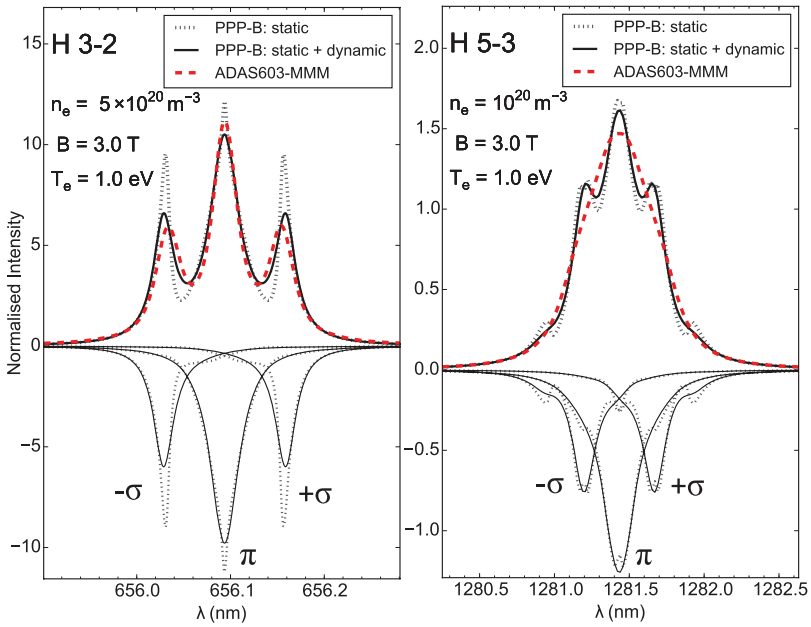

Figure 2. Comparison of H 3 → 2 and H 5 → 3 Stark–Zeeman line profiles generated with the PPP-B code (static and dynamic ions) and the simplified Stark–Zeeman model (ADAS603-MMM). Observation angle $\theta = 90°$. Separate π and σ polarisation components are shown below the abscissa.

PPP-B is carried out by first establishing the static profile, in which electrons are treated in the impact approximation and ions in the quasi-static approximation, with the static electric field integrated over the microfield distribution function and across the directions parallel and perpendicular to the magnetic field direction. The coupling in the π and σ components of the static Stark–Zeeman profile, as demonstrated in the H 3 → 2 example in figure 2, is evident in the profile asymmetries between the central π and shifted σ components (shown separately below the abscissa in figure 2). In the H 5 → 3 example (figure 2), the static Stark–Zeeman profile exhibits additional features in the line wings. Doppler broadening has not been included in figure 2 in order to isolate the pure Stark–Zeeman profiles. Ion dynamics are introduced at a later stage in the PPP-B calculation via a fluctuation rate parameter, $\nu = v_{th}/r_i$, where v_{th} is the ion thermal velocity and r_i is the mean distance between ions [22]. Ion dynamics can have a significant effect on the line shape, with large values of ν evolving towards the pure electron broadened profile as the ion perturbation becomes inefficient [22]. In figure 2 the introduction of ion dynamics, with $T_e = T_i = 1.0$ eV, is shown to have a significant smoothing effect on the static profiles.

In comparison to the PPP-B dynamic results, profiles generated with the proposed line profile model (denoted as ADAS603-MMM in figure 2), for which the main simplification is the separate treatment and subsequent convolution of the Stark and Zeeman effects, generally reproduce the line width and wing decay with sufficient accuracy, especially for high values of density. However, a loss in resolution of the line-centre features is evident for the β transitions, as well as a modest discrepancy in the σ-component shift in the α transitions. Good agreement was obtained for the higher-n lines for which the strong Stark contribution tends to smooth any Stark–Zeeman coupling effects.

Based on the above comparisons, we consider the proposed line profile model to be suitable for application to diagnostic studies and JET-ILW divertor measurements, with acknowledgement of likely higher uncertainties associated with recovering n_e using the β transitions. While both the standard method and the proposed line profile model are well suited to batch fitting of spectroscopic data (e.g. 500 CCD frames at 40 ms time resolution with 20 spatial bins processed in a few minutes for a single JET pulse), application of the PPP-B code for routine analysis is not currently feasible due to longer processing times (e.g. few minutes for a single Stark–Zeeman profile, depending on the transition and microfield grid resolution). Lastly, while we ignored the influence of higher effective charge on the Stark profile, a cursory investigation using the PPP-B code did not show this effect to be significant at divertor plasma densities, although previously reported simulation results [25] at high densities ($n_e > 10^{24}$ m^{-3}) in helium plasmas showed a 10% increase in the Stark FWHM for H 4 → 2.

2.2. Overview of diagnostics

Plasma density and electron temperature spectroscopic measurements were carried out using the recently upgraded mirror-linked JET-ILW divertor spectroscopy system [26, 27]. This includes: spectral coverage of the Balmer series (KT3A/B, spatially resolved, instrumental FWHM = 0.07 nm); Paschen series survey spectra up to D 5 → 3 (KT3D, outer divertor single LOS, instrumental FWHM ≈ 7 nm); D 4 → 3 filtered photodiodes (KT3D-PD, non-spectrally resolved, outer divertor single LOS). A medium resolution near-infrared spectrometer (instrumental FWHM = 0.24 nm) was also installed for a two week period in August 2014 in order to obtain higher resolution survey spectra of the D 5 → 3 line.

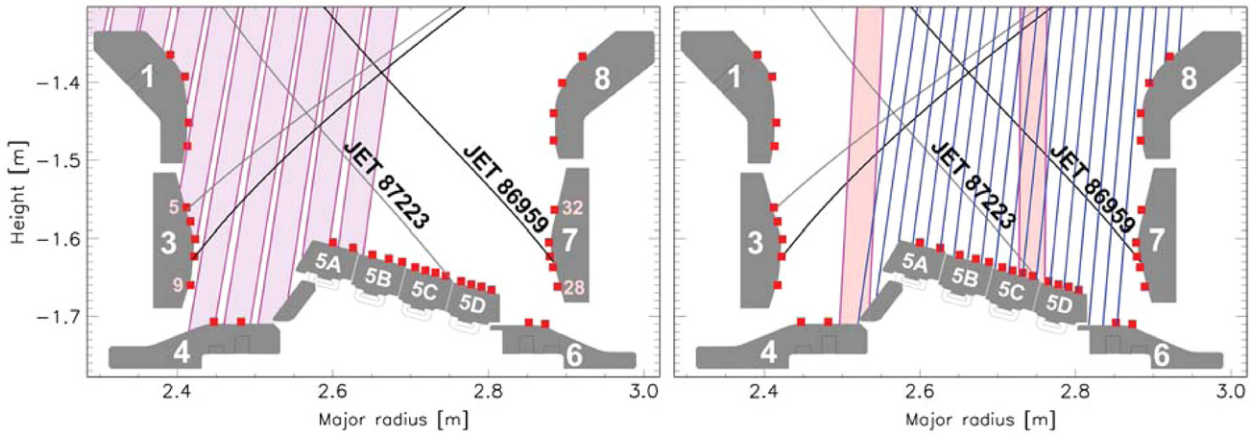

Figure 3. JET-ILW divertor geometry, tile identification and diagnostic views: Langmuir probes (KY4D) (red squares, with relevant probe numbers identified), high-resolution D $6 \rightarrow 2$ spectroscopy (KSRD) (left, shaded), selected chords from high-resolution D $3 \rightarrow 2$ spectroscopy (KSRB) (right, shaded), mirror-linked outer divertor imaging spectroscopy (KT3) (right, blue lines). Also shown are the horizontal (JET 87223, grey line) and vertical (JET 86959, black line) target plasma configurations as indicated by the location of the outer strike point.

In addition to the mirror-linked system, a fibre-fed high resolution spectroscopy system (KSRB/KSRD, instrumental FWHM $= 0.024$ nm) provided access to D $3 \rightarrow 2$ neutral VDF measurements in the outer divertor and density measurements from the D $6 \rightarrow 2$ line in the inner divertor. For these measurements the collecting optics are fitted with linear polarisers in order to isolate the π-polarisation component.

Fixed divertor Langmuir probes (KY4D) were used to corroborate the spectroscopic plasma density and electron temperature measurements with localised probe measurements. Figure 3 shows the relevant spectroscopic views, Langmuir probe (LP) locations, divertor geometry with tile identification, as well as the plasma configurations for the two plasma discharges considered.

2.3. Data evaluation

Spatially resolved density profiles in the radial coordinate across the outer divertor were inferred from Stark broadened Balmer (D $5 \rightarrow 2$, $7 \rightarrow 2$, $9 \rightarrow 2$) and Paschen (D $5 \rightarrow 3$) lines, depending on the mirror-linked spectroscopy setup, and signal-to-noise ratio (SNR). Density profiles across the inner divertor were inferred from the D $6 \rightarrow 2$ line measured with the high-resolution fibre-fed spectroscopy system. The simultaneous measurements of different transitions offered a basis for evaluating the robustness of the Stark model.

We employed the proposed simplified line profile model for least-squares fitting of the measured spectra, and, where appropriate, constrained the model with B-field values obtained from equilibrium reconstructions at the radial viewing chord location in the divertor. We also evaluated the impact of the Zeeman/Paschen-Back multiplet splitting on the Stark broadened profiles of the selected lines in the range of $2 \leqslant \mathrm{B} \leqslant 3.5$ T and $5 \times 10^{19} \leqslant n_\mathrm{e} \leqslant 10^{21}$ m^{-3} and found it to be negligible for the D $6 \rightarrow 2, 7 \rightarrow 2, 9 \rightarrow 2$ lines while the D $5 \rightarrow 2$ line exhibited modest sensitivity (up to 6% change in FWHM with an instrumental FWHM $= 0.07$ nm). The magnetic field effect on the D $5 \rightarrow 3$ line is significant (up to 20% change in FWHM with an instrumental FWHM $= 0.24$ nm), and therefore the B-field input value and relative intensities of the π and σ components is required to constrain the model. Since the spectrometer did not offer enough resolution to measure the component intensities directly and the optical train contains reflective, refractive and dichroic filter components which influence the effective transmission of each polarisation state, we inferred the σ/π ratio by comparing derived density values from the D $5 \rightarrow 3$ line to the Balmer lines and arrived at an estimate of $\sigma/\pi \approx 0.3$.

The influence of Doppler broadening on the set of measurement lines was also examined by varying the width of a single Gaussian component in the range $1 \leqslant T_\mathrm{n} \leqslant 10$ eV. The D $5 \rightarrow 3$ line was found to be weakly sensitive (5% change in FWHM with an instrumental FWHM $= 0.24$ nm), while the D $5 \rightarrow 2$ line exhibited higher sensitivity (20% change in FWHM with an instrumental FWHM $= 0.07$ nm). We therefore considered the D $5 \rightarrow 2$ line only for analysis of high density, low temperature detached plasmas for which we can ignore the Doppler contribution, although some broadening corresponding to a few eV from Frank–Condon dissociation energy of recycled D_2 molecules is likely present.

The low T_n sensitivity and the broad Stark profile of the D $5 \rightarrow 3$ line presents a good alternative to Balmer spectroscopy for density measurements due to less demanding spectral resolution requirements, while offering higher line emissivity relative to the high-n Balmer series lines. For example, the average Stark FWHM is broader by a factor of 6–8 compared to the D $5 \rightarrow 2$ line, while the total emissivity of the two lines is comparable, differing only by the spontaneous radiative rate coefficient. We estimate the uncertainty of inferred density values from the D $5 \rightarrow 3$ line to be within 25% due to insufficient knowledge of the σ/π polarisation component ratio compounded with the loss in resolution of the central line shape features using the simplified Stark–Zeeman–Doppler model.

Electron temperature radial profiles in detached plasma conditions were initially estimated using the high-n Balmer line spectra ($n_\mathrm{upper} = 9$–13) (see e.g. [8]) and the Saha-Boltzmann

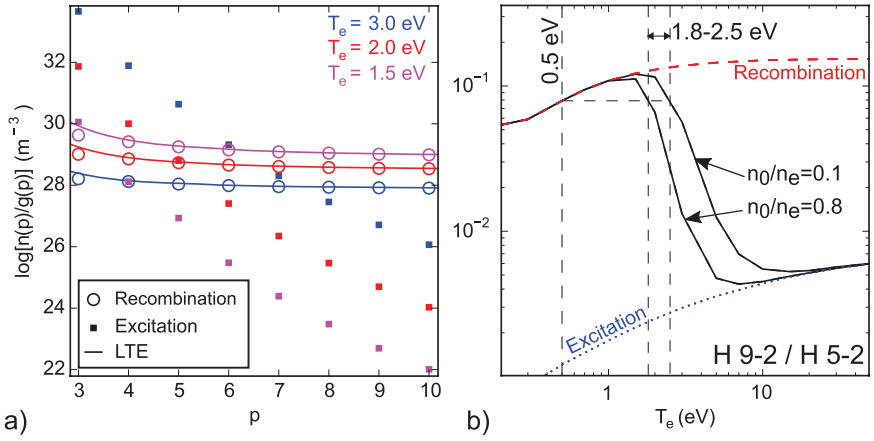

Figure 4. (*a*) Excitation and recombination components of H excited state populations (*p* denotes the upper level) calculated using ADAS PECs [13] for a neutral fraction $n_0/n_e = 0.5$. LTE populations evaluated using the Saha–Boltzmann distribution; (*b*) H $9 \rightarrow 2/5 \rightarrow 2$ intensity ratio calculated using ADAS PECs. Data evaluated at $n_e = 2 \times 10^{20}$ m^{-3}.

population distribution assuming local thermal equilibrium (LTE) (see e.g. [11]). The results yielded nonphysical values of T_e, however, most likely due to the influence of the photo-recombination continuum merging near the discrete-to-continuum (D–C) transition, as described in [28]. Since estimation of T_e depends on a theoretical model for the continuum baseline at the D–C transition, we focused instead on utilising the D $9 \rightarrow 2/5 \rightarrow 2$ intensity ratio. Other isolated lines (e.g. D $6 \rightarrow 2$, $7 \rightarrow 2$, $8 \rightarrow 2$) were not available on the outer divertor chords for the selected detached plasma discharge (and for similar discharges).

Although more accuracy is certainly gained by using multiple line ratios, useful information can be obtained from the D $9 \rightarrow 2/5 \rightarrow 2$ intensity ratio. Figure 4(*a*) shows the excited level population density (normalised to the statistical weight *g*) contributions due to excitation and recombination calculated using ADAS photon emissivity coefficients (PECs) [13] as well as the LTE populations using the Saha–Boltzmann distribution (see e.g. [18]). The contribution due to excitation is negligible for $n_{upper} > 5$ for $T_e < 2$ eV for any reasonable values of the neutral fraction n_0/n_e. Figure 4(*b*) shows the H $9 \rightarrow 2/5 \rightarrow 2$ line ratio sensitivity to T_e and the neutral fraction (the line ratio is also weakly sensitive to density, not shown for clarity). The limitation in using the single line ratio for T_e estimates is illustrated in figure 4(*b*) as it is possible for the measured line ratio value to correspond to different temperatures, if the extent of the excitation contribution is not known. An upper limit on T_e is thus placed (for example, 1.8–2.5 eV for the highlighted line ratio value for a neutral fraction range of 0.1–0.8), but without further information from additional lines, the lower T_e limit (0.5 eV in the highlighted example) corresponding to LTE conditions cannot be considered definitive. Nevertheless, we proceed with the assumption that the H $9 \rightarrow 2/5 \rightarrow 2$ line ratio is mainly driven by recombination processes in detached plasmas, as has been done in similar studies on Alcator C-Mod [11] and JET [29]. Improved coverage of Balmer lines from $n_{upper} = 3$ to 12 will be possible in future measurements as the enhanced mirror-linked divertor spectroscopy system [26, 27] on JET is fully commissioned, thus facilitating a more detailed investigation of the evolution of the excited populations and improved estimates of the T_e radial profiles.

LP current-voltage (I–V) characteristics for the selected plasma pulses were interpreted using a 4-parameter model accounting for sheath expansion (see [30]), or a 3-parameter model (see e.g. [31]) in cases where the four parameter model yielded unphysical T_e (and the derived $n_e \propto T_e^{-1/2}$) values due to increased scatter in the data points.

3. Measurement results and discussion

3.1. Comparison of Langmuir probe and spectroscopic measurements

The overestimation of T_e from LP measurements in high recycling and detached plasmas, and hence an underestimation of the derived n_e, is a well known observation. A possible explanation of this effect is based on the influence of hot upstream electrons, which can penetrate into the divertor plasma, on the probe I–V characteristics [32, 33]. A meaningful comparison of spectroscopically derived density values to LP measurements should therefore be carried out under fully attached plasma conditions characterised by a lack of significant parallel temperature and density gradients along the SOL. Typical upstream edge-SOL conditions in this case are $T_e \gtrsim 100$ eV and $n_e \lesssim 10^{19}$ m^{-3} in JET-ILW (see e.g. [34]), for which Stark broadening measurements in the divertor are prohibitive due to low SNR of the high-*n* lines and a significant Doppler contribution to the low-*n* line profiles. As such, we examined a horizontal outer target configuration discharge (JET 87223, $P_{NBI} = 7$ MW, $P_{ICRH} = 2.6$ MW and $I_p = 1.9$ MA) with midplane separatrix density and electron temperature values of $n_e \approx 1 - 2 \times 10^{19}$ m^{-3} and $T_e \approx 100$ –200 eV obtained from the core LIDAR Thomson scattering system. Divertor conditions in the time window of interest from $t = 10$–11 s determined from LPs near the outer strike point (OSP) were $n_e \approx 0.3 - 1.4 \times 10^{20}$ m^{-3} and $T_e \approx 10$ eV. Although at such SOL density and temperature gradients the divertor plasma is likely in the high recycling regime in which n_e underestimation from LPs is possible, the high recycling

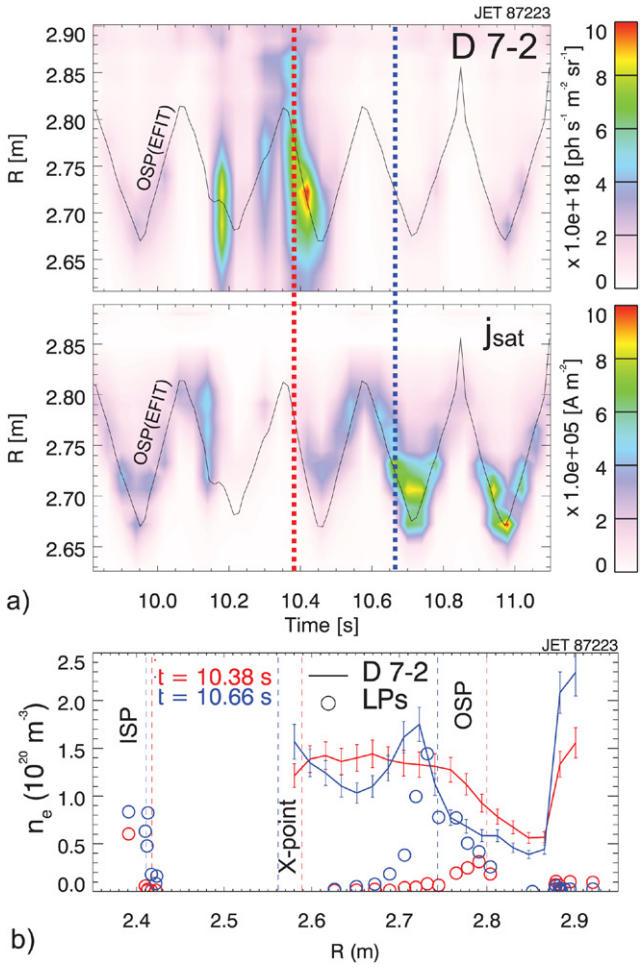

Figure 5. (*a*) Time evolution of outer divertor radial D 7 → 2 intensity and j_{sat} profiles; (*b*) radial density profiles from Stark broadening of D 7 → 2 line and LPs for JET pulse 87 223.

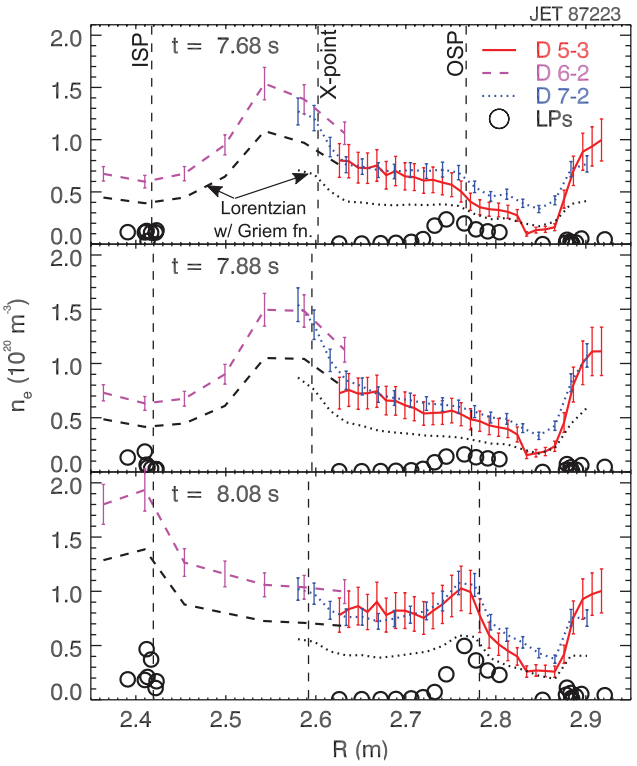

Figure 6. Radial density profiles from Stark broadening of D 5 → 3, 6 → 2 and 7 → 2 lines and localised density measurements from LPs for JET pulse 87 223.

rate on the horizontal tungsten tile 5 ensured sufficient SNR for the D 5 → 3, 6 → 2 and 7 → 2 lines which exhibited Stark broadening.

Figure 5(*a*) shows the time evolution of outer divertor radial profiles of the D 7 → 2 line intensity and j_{sat} from tile 5 LPs. The OSP position was swept along tile 5 at 4 Hz during this phase of the discharge. There is evidence of volume recombination at the outer divertor following a sawtooth crash at $t = 10.14$ s, as indicated by the sudden rise in the D 7 → 2 intensity as well as a rise in higher-n Paschen line intensities observed on the NIR low resolution survey spectrometer (not shown). This corresponds to a sudden drop in j_{sat} followed by its recovery and a corresponding collapse in the recombining plasma. Figure 5(*b*) compares the spectroscopically derived density profiles from D 7 → 2 Stark broadening and LP derived local density values. During the recombination phase ($t = 10.38$ s) the LP density values are significantly lower than the spectroscopically derived values. In the recovery phase ($t = 10.66$ s) where j_{sat} is high, there is better agreement particularly around the OSP.

The sudden rise in the spectroscopically derived density profile at $R > 2.88$ m is consistent with reflections on the tungsten coated tile 8, the curvature of which facilitates specular reflections from the inner divertor and/or the *X*-point emission and possibly from tile 5, depending on the plasma configuration. A detailed reflection analysis of the JET-ILW divertor is needed to predict the source of the reflected light. This feature is observed in most discharges and, compounded with the obstructed view of tile 7 by the mirror-linked spectroscopy system, makes density measurements at the OSP of vertical configuration discharges unreliable.

In an earlier ohmic phase of the discharge, the fixed horizontal OSP position facilitated the comparison of spectroscopically derived density profiles from three different spectral line measurements: D 5 → 3 (time resolution of 150 ms), D 7 → 2 (time resolution of 40 ms) and D 6 → 2 (time resolution of 100 ms). Figure 6 shows the density profiles for which the three separate spectroscopic measurements and LPs were interpolated along the time axis to account for the different exposure times. Good agreement is observed between the D 5 → 3 and D 7 → 2 profiles except for near $R = 2.85$ m where the D 5 → 3 density profile is markedly lower, likely as a result of increasing uncertainty in the line shape fitting procedure at low densities. Alternatively, it is possible that the D 5 → 3 and D 7 → 2 radiate in different regions along the LOS, and therefore provide a measure of density at different spatial locations. Good agreement is also evident in the overlap region near the *X*-point between the outer and inner density profiles, whereas LP measurements at both the inner and outer divertor underestimate the local density by a factor of 2–3 at the OSP and more so at the inner strike point (ISP).

Figure 6 also shows density profiles obtained by applying the standard method (Lorentzian coupled to the Griem density

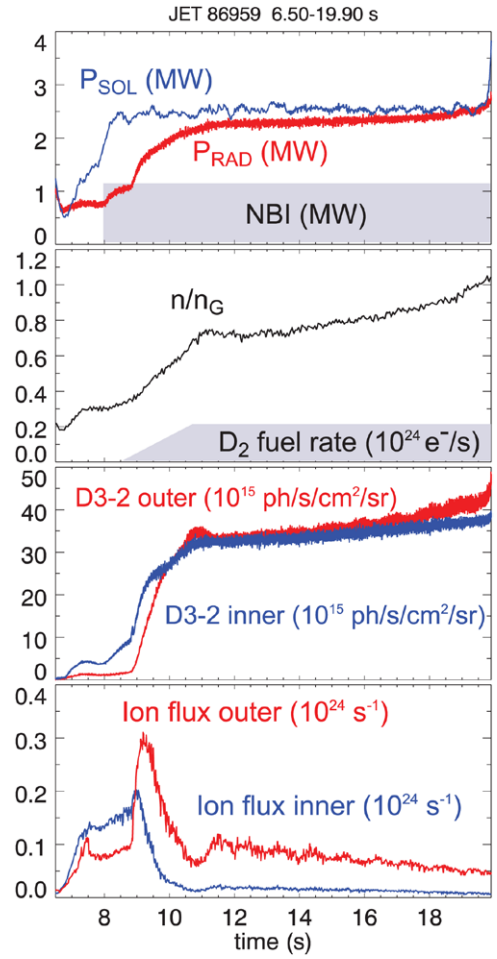

Figure 7. Time evolution of selected signals from JET pulse 86 959: estimated power entering the SOL, P_{SOL}; estimated total radiated power from bolometry, P_{RAD}; neutral beam (NBI) heating; the Greenwald density fraction, n/n_G; D_2 fuelling rate; total inner and outer D 3 → 2 intensity; and total ion flux on the inner and outer divertor targets.

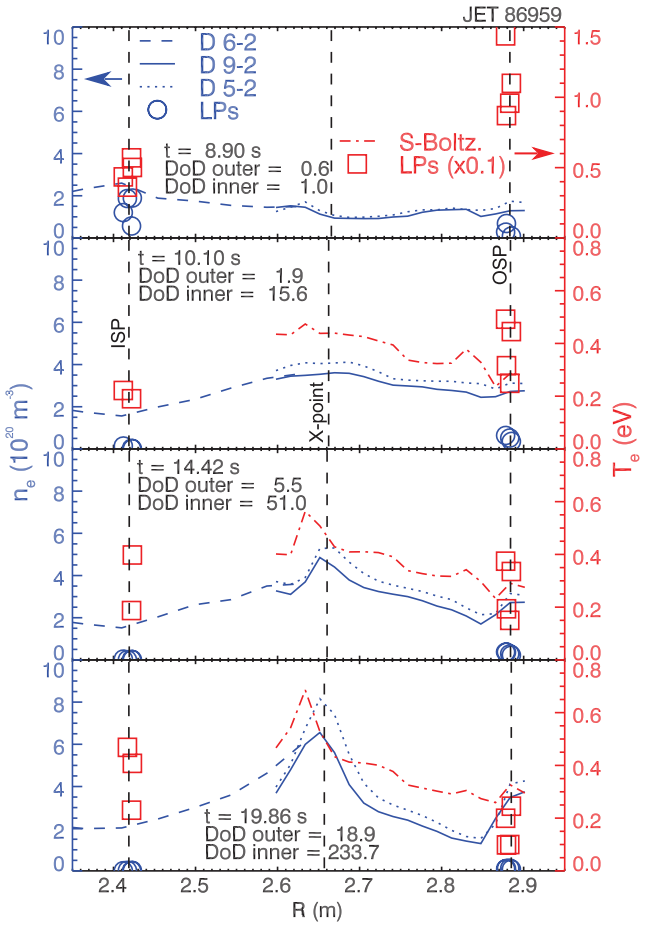

Figure 8. Radial density profiles from Stark broadening of D 5 → 2, 6 → 2, 9 → 2 lines and LPs, and electron temperature profile from D 9 → 2/5 → 2 line ratio for JET pulse 86 959. Electron temperature LP values scaled by 10^{-1} for clarity. ISP LPs include probes 5–8, OSP LPs include probes 29–32.

function) to the D 6 → 2 and D 7 → 2 spectral line shapes. In comparison to the density radial profiles obtained with the proposed simplified model, the standard method underestimates the density by approximately 20–40%.

General consistency in the spectroscopically derived density profiles (figure 6), in combination with the good agreement with LP results at $t = 10.66$ (figure 5) during the j_{sat} recovery phase, reinforce the suitability of the parametrised Stark broadening technique extending to lower-n lines, which must be additionally constrained with the B-field values to account for Zeeman splitting.

3.2. L-mode detached plasma measurements

In this section we consider an L-mode density limit discharge (pulse 86 959, figure 7; $B_T = 2.5$T, $I_p = 2.5$MA, $P_{NBI} = 1.2$MW, $P_{OHM} = 2.3$ MW, low-triangularity magnetic equilibrium and outer vertical target configuration) from a series of experiments aimed at examining the impact of the outer strike point configuration (horizontal versus vertical target) on divertor plasma conditions [35]. We utilized measurements of the the $n \geqslant 5$ Balmer lines for inferring plasma density. The density is ramped by puffing D_2 gas into the outer and inner divertor at constant input power starting at $t = 8.5$ s up to a steady state value of 2×10^{23} e^- s^{-1} at $t = 10.5$ s. The total ion flux to the outer target rises rapidly as the D_2 puffing rate increases, until at $t = 9.3$ s the characteristic roll-over is observed. At the inner target, the roll-over occurs slightly earlier at $t = 9.0$ s, shortly after the start of D_2 puffing. A sharp increase in the total radiated power P_{RAD}, as well as total D 3 → 2 intensity in the inner and outer divertor, is also observed after the start of puffing. The line-averaged mid-plane density rises steadily from 2.8×10^{19} m^{-3} to 8.9×10^{19} m^{-3} right before the density limit disruption terminates the pulse at $t = 20$ s. Volume recombination is observed shortly after the onset of fuelling as indicated by the signature recombination spectrum of the high-n Balmer lines.

We employed the 2-point SOL model density scaling [36] to estimate the degree of detachment (DoD) based on the integral ion flux to the inner and outer divertor, such that the plasma is considered partially detached for DoD $\lesssim 10$ and fully detached for DoD $\gtrsim 10$. The reference ion flux to density scaling is established in the time interval $t = 8.2$–8.8 s prior to the onset of fuelling and at constant P_{SOL}.

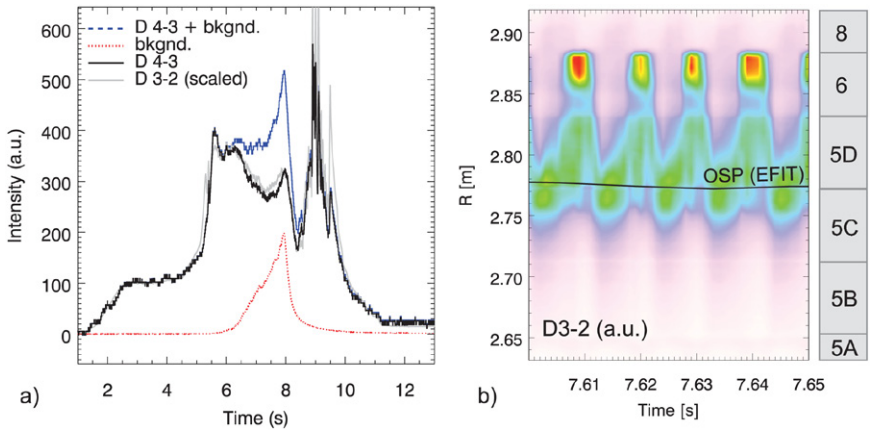

Figure 9. JET pulse 86 718 (*a*) total D 4 → 3 intensity on outer divertor and thermal background contribution; total D 3 → 2 intensity; (*b*) ELM-resolved time evolution of radial D 3 → 2 intensity profiles and radial field-of-view of the outer divertor (see tile geometry in figure 3).

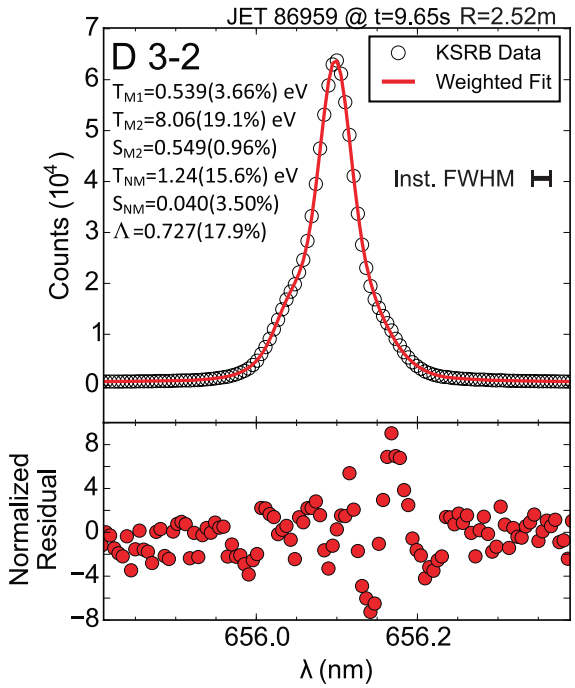

Figure 10. Example of neutral VDF parametric fit to divertor D 3 → 2 measured line profile for JET pulse 86 959, $t = 9.65$ s, $R = 2.54$ m. Parameter estimates and fit error estimates shown.

Table 2. Input parameters and range of values for multi-parametric fitting of synthetic diagnostic spectral line profiles.

Fit parameter	Range	Units
n_e	5.0–50.0	10^{19} m^{-3}
T_{M1}	0.5–5.0	eV
T_{M2}	5.0–20.0	eV
T_{NM}	1.5–5.0	eV
S_{M2}	0.4–0.6	—
S_{NM}	0.00–0.05	—
Λ	0.656 (fixed)	nm
B	2.5–4.5	Tesla
$T/(T+D)$	0.2–0.5	—

Figure 8 shows spectroscopically derived plasma radial density and local LP derived values. We ignored any neutral temperature contribution to the D 5 → 2 line profile which could account for the modest discrepancy observed between the D 9 → 2 and 5 → 2 profiles. The overlap region between the inner and outer profiles is again in good agreement. The radial profile values right near the OSP at $R > 2.85$ m are considered unreliable due to shadowing of tile 7 and reflections on tile 8 (see figure 3).

At $t = 8.9$ s, corresponding to the start of the fuelling ramp and before the ion flux roll-over, there is a gradual density increase from the *X*-point towards the ISP and OSP, indicating high recycling conditions consistent with DoD-inner and DoD-outer $\leqslant 1$. LP density values in this regime are in relatively good agreement with the spectroscopically derived density values near the strike points. LP T_e values are between 10–15 eV. The spectroscopically derived T_e profile is not available since application of the Saha–Boltzmann distribution to the D 9 → 2/5 → 2 ratio is not valid in this temperature range due to the influence of exitation fluxes on the upper state populations (see figure 4). At $t = 10.10$ s after the ion flux roll-over, DoD-inner > 10 indicating full detachment, while the outer divertor is partially detached (DoD-outer = 1.9). The density decreases gradually away from the *X*-point towards the ISP and OSP and the LP density measurements at the strike points are significantly underestimated. Spectroscopic T_e estimates are between 04–0.6 eV (assuming LTE conditions), much lower than LP values at the OSP, indicating significant overestimation of LP T_e results. At $t = 14.42$ s the density near the *X*-point rises and the profile begins to exhibit a well defined peak while the density continues to decrease towards the OSP. This is consistent with the incursion of the dense plasma away from the strike point and towards the *X*-point, as has been observed in previous radial density profile measurements in [8]. A peak in the temperature profile is also evident. We note that, since the outermost spectroscopic chords are susceptible to reflections, direct n_e and T_e measurements at $R > 2.86$ m at the OSP were not possible. At $t = 19.86$ s, shortly before the density limit disruption, both the outer and

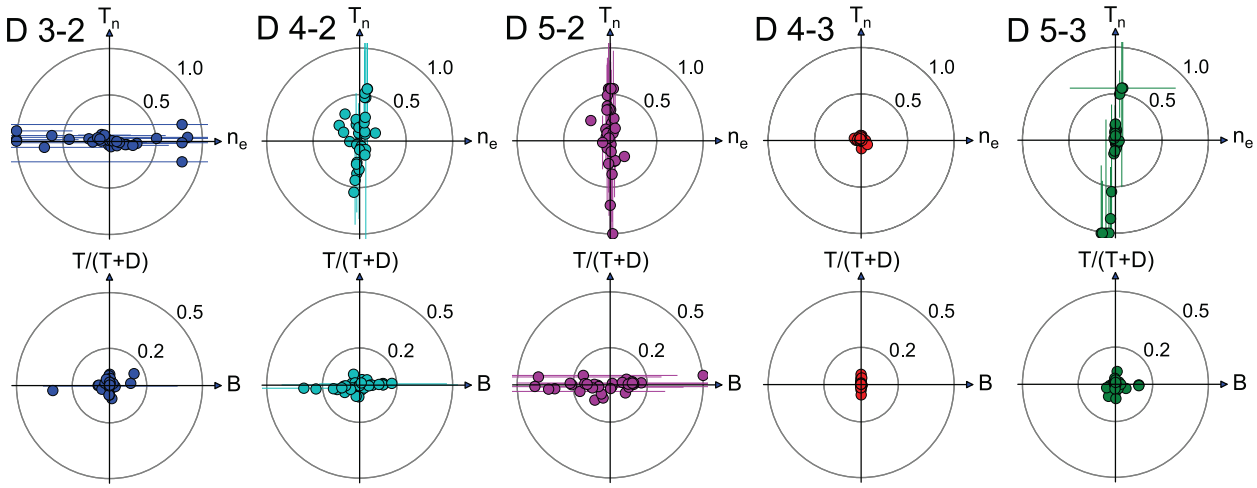

Figure 11. Simulation results for 4-parameter fits for the D 3 → 2, 4 → 2, 5 → 2, 4 → 3, and 5 → 3 lines. Each marker corresponds to a simulation case and its position to the relative difference between the fit estimate and input value. Fit error bars <25% are not shown for clarity.

inner divertor are completely detached and the density peak increases further, consistent with the radiation pattern during MARFE formation(see e.g. [2]), while density along the outer leg continues to fall. Changes in the T_e profile are less pronounced compared to relatively strong shaping in the density profile.

Observations of increased detachment stability and extended MARFE lifetime have recently been reported in JET-ILW detachment experiments [2] and present increased opportunity for feedback control to stabilise the detached operating regime (see e.g. [3] for previous attempts using edge density as feedback signal). Balmer–Paschen series divertor spectroscopy is well suited for monitoring volume recombination and the incursion of the dense plasma into the *X*-point region. In addition to line ratios which exhibit sensitivity to volume recombination processes (e.g. D 5 → 2/D 3 → 2), n_e radial profiles offer a good measure of density gradients associated with the MARFE formation near the *X*-point, as demonstrated in figure 8. By replacing the least-squares fitting technique with computationally efficient look-up tables based on a 2-point estimate of the line FWHM and using the parametrised MMM Stark broadening coefficients in table 1, estimates of n_e profiles for feedback control should be feasible within the existing real-time interface of the mirror-linked divertor spectroscopy system.

3.3. Assessment of the influence of thermal background emission on Paschen line intensity measurements

Maximum surface temperatures of the JET-ILW tungsten divertor target lamellae have been observed to exceed 1000 °C due to steady-state and transient heat loading [37]. We examined the impact of thermal emission on the mirror-linked divertor spectroscopy measurements of the Paschen lines using the low resolution NIR spectrometer and the pair of filtered NIR photodiodes (KT3D-PD) which measure the contribution of the thermal continuum on the D 4 → 3 line intensity over the outer divertor (single LOS, see [27] for details). We scanned the range of pulses throughout the 2014 campaign, with emphasis on horizontal target (tile 5) plasma configurations, and found that the thermal background continuum was significant for high input power discharges ($P_{NBI} > 20$ MW) and attached divertor plasma conditions. The overall effect on the D 5 → 3 line was increased shot noise, typically by a factor $\leqslant \sqrt{2}$. The highest thermal contribution to the D 4 → 3 line intensity was observed in pulse 86 718 ($P_{NBI} = 22.7$ MW, $I_p = 2$ MA), shown in figure 9(*a*). Figure 9(*b*) shows high spatial and time resolution measurements of D 3 → 2 line intensity (see KT3-E8TA filtered imaging diagnostic in [27]) at $t = 7.60$–7.65 s near the peak thermal continuum emission with $T_{max} = 1190$ °C. The emission is localised at the strike point, shifting outward towards tile 6 during each ELM cycle. This indicates that the volume integrated D 4 → 3 measurement is representative of the localised thermal contribution. At the thermal peak, the D 4 → 3 to thermal background intensity ratio is ≈1.7. The total D 3 → 2 outer divertor intensity shown in figure 9(*a*) is also consistent with the background corrected D 4 → 3 line intensity. Therefore we consider measurements of the D 4 → 3 line in the JET-ILW environment to be feasible, even at high background surface temperatures, albeit with a modest decrease in the SNR.

4. Multi-parametric fitting of low-*n* line profiles

Whereas the $n \geqslant 5$ Balmer lines are used routinely for n_e, T_e determination and as indicator of the extent of volume recombination in detached plasmas, the low-*n* Balmer and Paschen lines offer additional diagnostic capabilities since, given sufficient instrument resolutions, their spectral profiles contain information on the *B*-field magnitude, isotope ratio, the neutral VDF as well as plasma density. In this section we examine the scope for parameter recovery from the low-*n* Balmer and Paschen lines using a survey of synthetic diagnostic data generated with the simplified line profile model and assuming a localised divertor emission source consistent with JET-ILW vertical view observations.

4.1. Simulation setup

We generated synthetic diagnostic data for the D $3 \rightarrow 2$, $4 \rightarrow 2$, $5 \rightarrow 2$, $4 \rightarrow 3$, $5 \rightarrow 3$ lines using instrument characteristics which correspond to a high resolution spectroscopy configuration with a linear dispersion of 0.0075 nm pixel^{-1} and an instrumental FWHM = 0.02 nm. Zeeman polarisation component filtering is not applied to the synthetic data in order to asses the entire line profile including the magnetic field effects. We note that there are currently no existing capabilities for measuring the D $4 \rightarrow 3$ line profile on JET-ILW, hence the following analysis serves as a basis for evaluating its properties.

Photon shot noise and camera electronic noise, σ_e, are added to the synthetic data such that the SNR $= I_{max}/\sqrt{(I_{max} + \sigma_e^2)}$ corresponds to good photon statistics with a chosen value of 150. The synthetic data is generated by randomly sampling the line profile at each pixel position according to a normal distribution with the standard deviation corresponding to the total noise term. The input parameters that define the line profile are recovered via a non-linear least squares fitting routine which minimises χ^2 using the Levenberg–Marquardt algorithm [38], weighted by the variances of the pixel intensity values.

We draw on the spectroscopic and LP measurement results to establish an appropriate range of values for n_e. Since the Stark broadening contribution is only weakly dependent on T_e, and, treating electron and ion temperatures as equal in our model, we assumed $T_e = 1$ eV for high density detached plasmas and $T_e = 5$ eV for high-recycling and attached plasmas.

To elucidate the appropriate selection of Maxwellian and non-Maxwellian neutral temperatures and their relative contributions to the total VDF (thus capturing contributions from charge exchange of hot background plasma ions with cold recycled neutrals and reflection of fast atoms), we examined D $3 \rightarrow 2$ divertor spectra for JET discharges 87 223 (high recycling) and 86 959 (detached) measured by the fibre-fed π-component filtered spectroscopy system (see figure 3). The neutral VDF is estimated using the Kukushkin model, which has previously been applied in JET-ILW SOL measurements using midplane views [5]. The interpretation is more straightforward for the divertor chords compared to the midplane radial and tangential chords due to the σ-component blocking and the absence of significant stray light.

We defined the neutral VDF model to be composed of: a single non-Maxwellian component with statistical weight S_{NM}, temperature T_{NM} and the damping parameter Λ which quantifies the attenuation of the inward flux (see [14] for details); two Maxwellian components parametrised together with the statistical weights S_{M1}, S_{M2} and corresponding temperatures T_{M1} and T_{M2}. Figure 10 shows an example of the weighted fit for pulse 86 959 at $t = 9.65$ s and $R = 2.52$ m with parameter estimates and standard errors. The majority of the normalised residuals are within ± 2, indicating a good fit, except for a statistically significant peak in the red wing which is not accounted for by the model. Similar fit quality was obtained for pulse 87 223, $t = 8.45$ s, $R = 2.74$ m, but with a negligible non-Maxwellian contribution, and higher Maxwellian temperatures ($T_{M1} = 18$ eV, $T_{M2} = 2.5$ eV and $S_{M2} = 0.5$). From these results, we consider the model to be a reasonably good representation of the LOS integrated neutral VDF in the JET-ILW divertor for the selected pulses and we therefore defined the neutral VDF contribution in the multi-parameteric fitting analysis on this basis. Table 2 summarises the input parameters that describe the total line profile and their range of values considered for the analysis.

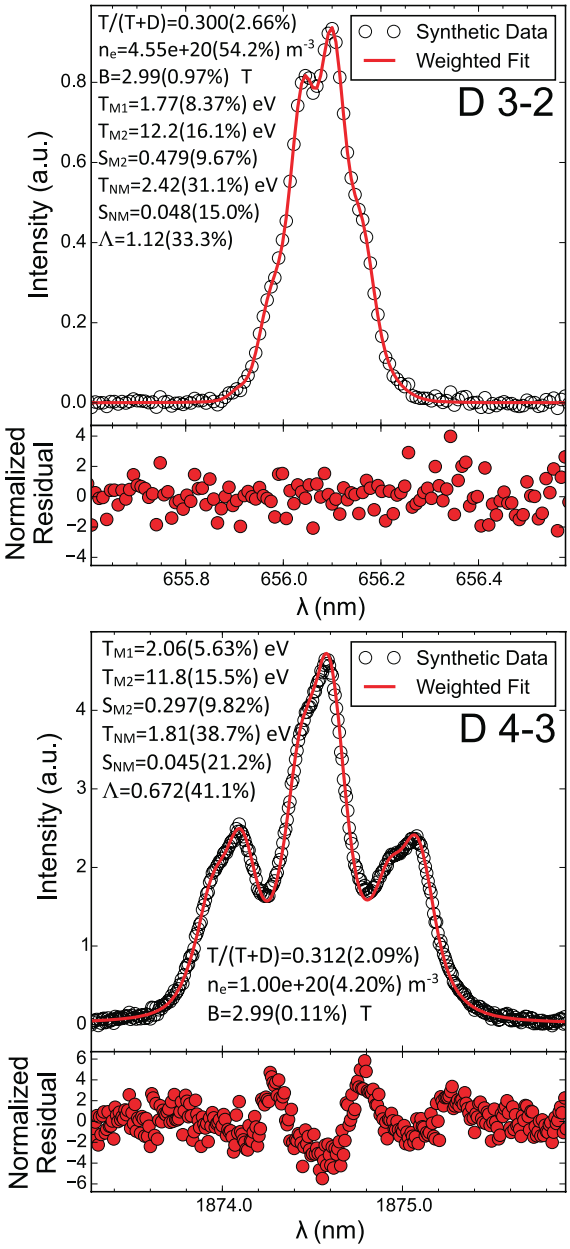

Figure 12. Example of parametric fits to synthetic diagnostic D $3 \rightarrow 2$, $4 \rightarrow 3$ high resolution line profile data with observation angle $\theta = 90°$. Fit parameter and error estimates shown for input vales: $T/(T + D) = 0.300$, $B = 3.00$ T, $n_e = 1.00 \times 10^{20}$ m^{-3}, $T_{M1} = 1.50$ eV, $T_{M2} = 10.0$ eV, $S_{M2} = 0.500$, $T_{NM} = 1.50$ eV, $S_{NM} = 0.050$, $\Lambda = 0.656$ nm.

4.2. Simulation results and discussion

In the first iteration, multi-parametric fits were carried out for each line by varying the input parameters n_e, B and the tritium

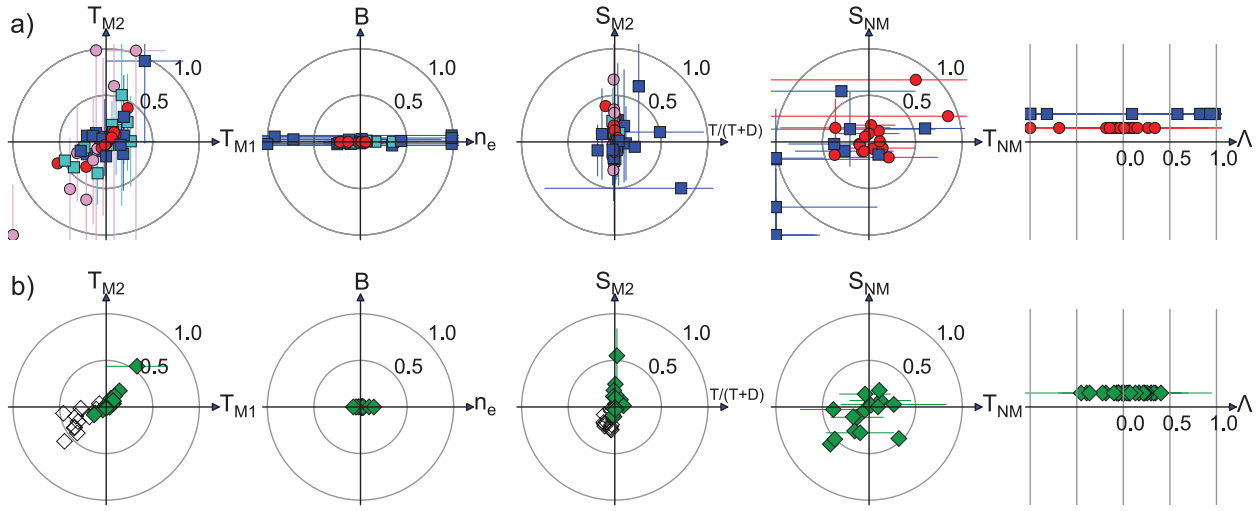

Figure 13. Simulation results for 9-parameter fits for (*a*) isolated D 3 → 2 (squares: high-density, light blue; low-density, dark blue) and D 4 → 3 (circles: high-density, purple; low-density, red) lines; (*b*) combined D 3 → 2, 4 → 3 line profiles (high-density, open symbols; low-density, green). Each marker corresponds to a simulation case and its position to the relative difference between the fit estimate and input value. Fit error bars <25% are not shown for clarity.

fraction $T/(T+D)$ in the range according to table 2 and using a simplified neutral VDF described by a single Gaussian and $1 \leqslant T_n \leqslant 10$ eV. The fit precision and accuracy results for each line are presented in figure 11, where each marker corresponds to a simulation case and its position to the relative difference between the model input value and the free parameter estimate and associated standard error. The best results were obtained for the D 4 → 3 line with parameter estimates for all cases recovered within 10% of their input values. The D 3 → 2 results show poor sensitivity to Stark broadening, especially for cases with $n_e < 10^{20}$ m^{-3}. Conversely, the D 4 → 2, 5 → 2 and 5 → 3 line results show decreased sensitivity to T_n and increased sensitivity to n_e. Parameter recovery from D 3 → 2 and 4 → 3 is generally more sensitive to B and $T/(T+D)$. Overall, the synthetic diagnostic fitting results indicate that in the absence of additional information to constrain the fit, the D 4 → 3 line offers increased scope for recovery of plasma parameters from spectroscopic observations. This is consistent with the wavelength scaling of the broadening and splitting mechanisms according to the transition energy (center wavelength λ_p) of the Balmer and Paschen series lines such that: Doppler broadening $\Delta\lambda_{1/2} \propto \lambda_p\sqrt{k_B T_n/m_a}$, where m_a is the mass of the emitters; Zeeman component separation $\Delta\lambda \propto \lambda_p^2 B$; and the D–T isotopic separation from the Rydberg formula $\Delta\lambda \propto \lambda_p$. Thus, relative to the D 3 → 2 line at 656 nm, Doppler broadening for the D 4 → 3 line (1874.6 nm) is ×2.9 wider for the same neutral temperature, as is the D–T separation. The quadratic wavelength dependence on the Zeeman splitting leads to a $\pi - \sigma$ separation that is ×8.4 greater, whereas the pure Stark broadening FWHM is wider by a factor of ≈13.5. Hence measurements of the D 4 → 3 profile offer reduced spectral resolution requirements, however, the shift in emphasis in wavelength space towards the Stark broadening contribution may also reduce the scope for recovery of more complex neutral VDFs at high densities.

To further examine the diagnostic capabilities of the D 3 → 2 and 4 → 3 lines we considered the more representative neutral VDF according to table 2. The second iteration of the multi-parametric fitting analysis thus included 9 free parameters: B, $T/(T+D)$, n_e, S_{M2}, T_{M1}, T_{M2}, S_{NM}, T_{NM}, Λ, where the first Maxwellian statistical weight is then derived from $S_{M1} = 1 - S_{M2} - S_{NM}$. Figure 12 shows an example of the synthetic diagnostic data and the line of best fit for the D 3 → 2 and 4 → 3 lines.

Plasma parameter sets corresponding to attached, high-recycling and detached divertor plasma conditions were selected comprising 27 simulation cases. The relative differences between the free parameter fit estimates and their input values for low density ($n_e \leqslant 10^{20}$ m^{-3}) and high density ($n_e > 10^{20}$ m^{-3}) cases are presented in figure 13(*a*). Since the non-Maxwellian contribution in the given range has only a small contribution to the total line profile, it is the most difficult feature to recover, especially for the D 4 → 3 line. We removed this contribution from the set of input parameters in the high density cases due to poor sensitivity, large fit uncertainties (>100%) for S_{NM}, T_{NM}, and Λ and to ensure faster solution convergence. Comparing the D 4 → 3 results to the first iteration (figure 11), the increased number of parameters has clearly degraded the parameter recovery, especially for the neutral temperature components at high density and conversely low temperature ($T_{M1} < 1.5$ eV, $T_{M2} < 7.5$ eV). At low densities the D 4 → 3 parameter recovery is generally more accurate, whereas the D 3 → 2 results show more scatter and larger fit uncertainties, especially in n_e, S_{NM} and T_{NM}. The quality of the fits shift in favour of the D 3 → 2 line at high densities due to improved sensitivity to Stark broadening, while the sensitivity to low neutral temperatures remains sufficient for the T_{M1}, T_{M2} fit estimates to fall within 50% and S_{M2} within 20% of the input values.

Given the inverse relationship between fit quality of the isolated D 3 → 2 and 4 → 3 lines in high versus low density

conditions (and conversely, low versus high neutral temperatures), coupling the two profiles takes advantage of each line's sensitivity, thus improving the overall recovery of parameters as shown in figure 13(*b*) for the same set of simulation cases and input parameters. The results show a marked improvement in the fit accuracy and estimated parameter uncertainty for all 9 input parameters, while some degree of systematic error and parameter estimate correlation is also evident in the recovered values of T_{M1} and T_{M2} at high densities and low temperatures.

The results of the above analysis demonstrate the difficulties associated with recovering information from an isolated low-n hydrogen spectral line characterised by a large set of input parameters, and highlight the potential for substantial improvement in parameter recovery through simultaneous minimization of the D $3 \rightarrow 2$ and $4 \rightarrow 3$ line profiles.

5. Conclusions

In surveying the hydrogenic Balmer and Paschen series spectral lines, we have considered both the existing measurement capabilities on JET-ILW as well as an assessment of the scope for parameter recovery from low-n lines using high resolution synthetic diagnostic data.

We formulated a model of the line profiles up to $n = 9$ accounting for the Zeeman, Stark and Doppler contributions while neglecting any coupling of the magnetic and electric field effects. Compared to the coupled Stark–Zeeman PPP-B code, the proposed model reproduced the spectral profile features, including the line FWHM and wing decay, with good accuracy especially at high densities and for high-n transitions. For the low-n lines, and particularly the β transitions, some loss of resolution near the line center was evident. Likewise, the σ-component shifts and asymmetries in the D $3 \rightarrow 2$ and $4 \rightarrow 3$ lines arising from Stark–Zeeman coupling could not be fully reproduced with the simplified model. However, the computational efficiency of the proposed model makes it more suitable for batch analysis of spectroscopy data and possibly for real-time measurements of divertor density gradients based on observations of progressively peaked profiles near the *X*-point in the L-mode density limit discharge.

Comparisons of LP measurements to spectroscopically derived plasma density and temperature profiles confirm the overestimation (understimation) of electron temperature (density) values obtained with LPs in high recycling and detached conditions and reinforce the critical role of passive spectroscopy diagnostics in this regime. First time application of the D $5 \rightarrow 3$ line for inferring n_e yielded good agreement with Stark broadened D $7 \rightarrow 2$ and $6 \rightarrow 2$ lines, but due to insufficient instrument resolution for direct measurement of the σ/π component ratio, measurements for $n_e < 5 \times 10^{19}$ m^{-3} were less accurate. Due to the low T_n sensitivity and broader Stark contribution, the D $5 \rightarrow 3$ line profile characteristics offer potential for fast density measurements at relatively low spectral resolution.

Multi-parametric fitting simulations to synthetic diagnostic spectral data for isolated low-n Balmer and Paschen lines across a range of divertor plasma conditions showed particularly good parameter recovery from the convolved data (within 10%) for the D $4 \rightarrow 3$ line for cases with a simplified single Maxwellian neutral VDF, while the D $4 \rightarrow 2$ and $5 \rightarrow 2$ exhibited poor sensitivity to recovery of the neutral temperature and magnetic field. The accuracy and precision of the recovered parameters for D $3 \rightarrow 2$ and $4 \rightarrow 3$ lines was markedly degraded once we considered a more representative multi-component neutral VDF contribution which increased the total number of free parameters from 4 to 9. By simultaneously fitting both D $3 \rightarrow 2$ and $4 \rightarrow 3$ profiles we obtained significant improvement in fit quality for all 9 parameters, but at high densities the fits were largely insensitive to the small non-Maxwellian neutral temperature contribution. The results of the synthetic data fitting analysis highlight the benefits of complementary measurements of low-n line spectra, from which significant plasma parameter information can be extracted. Although quantitative measurements of the D $4 \rightarrow 3$ (1874.6 nm) line profile are currently not available, the increased scope for feature resolution and for comparison to theoretical Stark–Zeeman line profile models presents a good case for its inclusion in future diagnostics.

Acknowledgments

This work has been carried out within the framework of the EUROfusion Consortium and has received funding from the Euratom research and training programme 2014-2018 under grant agreement No 633053. The views and opinions expressed herein do not necessarily reflect those of the European Commission. This work was also partly funded by the United Kingdom Engineering and Physical Research Council under Grant No. EP/K504178/1.

References

[1] Ikeda K. 2007 *Nucl. Fusion* **47** S203
[2] Huber A. *et al* 2013 *J. Nucl. Mater.* **438** S139–47
[3] Brezinsek S. *et al* 2009 *J. Nucl. Mater.* **390–1** 267–73
[4] Matthews G.F. *et al* 2011 *Phys. Scr.* **T145** 014001
[5] Kukushkin A.B. *et al* 2014 *Proc. 25th IAEA Fusion Energy Conf. (St. Petersburg, Russia)* www-pub.iaea.org/iaeameetings/46091/25th-Fusion-Energy-Conference-FEC-2014
[6] Kubo H. *et al* 2000 *Proc. Int. Seminar on Atomic Processes in Plasmas* (Japan: National Institute for Fusion Science) pp 65–8
[7] Meigs A.G. *et al* 1998 *Proc. 25th EPS Conf. on Plasma Physics (Prague, Czech Republic)* pp P–1.017 http://epsppd.epfl.ch/Praha/start.htm
[8] Meigs A. *et al* 2013 *J. Nucl. Mater.* **438** S607–11
[9] Potzel S., Dux R., Müller H.W., Scarabosio A. and Wischmeier M. 2014 *Plasma Phys. Control. Fusion* **56** 025010
[10] Soukhanovskii V.A., Johnson D.W., Kaita R. and Roquemore L. 2006 *Rev. Sci. Instrum.* **77** 10F127
[11] Lumma D., Terry J.L. and Lipschultz B. 1997 *Phys. Plasmas* **4** 2555–66
[12] Griem H.R. 1974 *Spectral Line Broadening by Plasmas* (London: Academic)

[13] Summers H. 2004 *The ADAS User Manual* version 2.6 (www.adas.ac.uk)
[14] Kukushkin A.B. *et al* 2014 *J. Phys.: Conf. Ser.* **548** 012012
[15] Frisch U. and Brissaud A. 1971 *J. Quant. Spectrosc. Radiat. Transfer* **11** 1753–66
[16] Stehlé C. and Hutcheon R. 1999 *Astron. Astrophys. Suppl. Ser.* **140** 93–7
[17] Griem H.R. 1997 *Principles of Plasma Spectroscopy* (Cambridge: Cambridge University)
[18] Kunze H.J. 2009 *Introduction to Plasma Spectroscopy* (Berlin: Springer)
[19] Holtsmark J. 1919 *Ann. Phys.* **363** 577–630
[20] Wujec T., Olchawa W., Halenka J. and Musielok J. 2002 *Phys. Rev.* E **66** 066403
[21] Ferri S. *et al* 2014 *Atoms* **2** 299–318
[22] Ferri S. *et al* 2011 *Phys. Rev.* E **84** 026407
[23] Talin B. *et al* 1995 *Phys. Rev.* A **51** 1918–28
[24] Calisti A. *et al* 2010 *Phys. Rev.* E **81** 16406
[25] Halenka J., Olchawa W., Grabowski B. and Gajda F. 2002 *J. Quant. Spectrosc. Radiat. Transfer* **74** 539–44
[26] Meigs A., Stamp M., Igreja R., Sanders S. and Heesterman P. 2010 *Rev. Sci. Instrum.* **81** 10E532
[27] Lomanowski B.A. *et al* 2014 *Rev. Sci. Instrum.* **85** 11E432
[28] Pigarov A.Y., Terry J.L. and Lipschultz B. 1998 *Plasma Phys. Control. Fusion* **40** 2055–72
[29] McCracken G. *et al* 1998 *Nucl. Fusion* **38** 619
[30] Gunn J.P., Boucher C., Stansfield B.L. and Savoie S. 1995 *Rev. Sci. Instrum.* **66** 154–9
[31] Wesson J. 2004 *Tokamaks* 3rd edn (Oxford: Clarendon)
[32] Horacek J. *et al* 2003 *J. Nucl. Mater.* **313–6** 931–5
[33] Stangeby P. 1995 *Plasma Phys. Control. Fusion* **37** 1031–7
[34] Duran I. *et al* 2015 *J. Nucl. Mater*. **463** 432–5
[35] Groth M. *et al* 2015 *J. Nucl. Mater.* **463** 471–6
[36] Loarte A. *et al* 1998 *Nucl. Fusion* **38** 331
[37] Balboa I. *et al* 2012 *Rev. Sci. Instrum.* **83** 100530
[38] Press W.H., Flannery B.P., Teukolsky S.A. and Vetterlin W.T. 1986 *Numerical Recipies* 1st edn (Cambridge: Cambridge University)